Event-Related Phase Synchronization Propagates Rapidly across Human Ventral Visual Cortex

Oscar Woolnough[1,2], Kiefer J. Forseth[1,2], Patrick S. Rollo[1,2], Zachary J. Roccaforte[1,2], Nitin Tandon[1,2,3,*]

[1] Vivian L. Smith Department of Neurosurgery, McGovern Medical School at UT Health Houston, Houston, TX, 77030, United States of America

[2] Texas Institute for Restorative Neurotechnologies, University of Texas Health Science Center at Houston, Houston, TX, 77030, United States of America

[3] Memorial Hermann Hospital, Texas Medical Center, Houston, TX, 77030, United States of America

* Correspondence: nitin.tandon@uth.tmc.edu

1 Abstract

2 Visual inputs to early visual cortex integrate with semantic, linguistic and memory inputs in higher
3 visual cortex, in a manner that is rapid and accurate, and enables complex computations such as face
4 recognition and word reading. This implies the existence of fundamental organizational principles
5 that enable such efficiency. To elaborate on this, we performed intracranial recordings in 82
6 individuals while they performed tasks of varying visual and cognitive complexity. We discovered that
7 visual inputs induce highly organized posterior-to-anterior propagating patterns of phase modulation
8 across the ventral occipitotemporal cortex. At individual electrodes there was a stereotyped
9 temporal pattern of phase progression following both stimulus onset and offset, consistent across
10 trials and tasks. The phase of low frequency activity in anterior regions was predicted by the prior
11 phase in posterior cortical regions. This spatiotemporal propagation of phase likely serves as a feed-
12 forward organizational influence enabling the integration of information across the ventral visual
13 stream. This phase modulation manifests as the early components of the event related potential;
14 one of the most commonly used measures in human electrophysiology. These findings illuminate
15 fundamental organizational principles of the higher order visual system that enable the rapid
16 recognition and characterization of a variety of inputs.

Introduction

Ventral occipitotemporal cortex is organized in a cortical hierarchy from early visual regions (e.g. calcarine cortex) to associative areas (e.g. fusiform cortex) (Felleman and Van Essen, 1991; Morán et al., 1987), that constitutes the ventral visual stream (Mishkin et al., 1983). This processing pathway is crucial for the integration of visual processing with language and memory (Forseth et al., 2018; Ghuman et al., 2014; Hirshorn et al., 2016; Kadipasaoglu et al., 2016; Tang et al., 2014; Woolnough et al., 2021b), but it is unclear how the propagation of information between functional components of the human ventral visual pathway is coordinated.

Recently, spatial propagation of information has been characterized, in both humans and non-human primates, as travelling waves of cortical activation. These occur at both the macro and micro scale and represent the structured propagation of information across the cortical surface in response to inputs (Lozano-Soldevilla and VanRullen, 2019; Muller et al., 2018, 2014; Sato et al., 2012) or may occur spontaneously (Bahramisharif et al., 2013; Davis et al., 2020; Halgren et al., 2019; Muller et al., 2016; Zhang et al., 2018). In the ventral visual stream of macaques this manifests as a rapid feedforward sweep of activation following visual stimulation (Lamme and Roelfsema, 2000). This spatiotemporal organization, manifest as a travelling wave indexes synchronized long-range cortico-cortical connections, enabling the integration of information across multiple cortical areas (Sato et al., 2012; Zhang et al., 2018) and perhaps also facilitates predictive coding (Alamia and VanRullen, 2019; Arnal and Giraud, 2012). Such travelling waves have commonly been characterized as a spatial propagation of phase. Sensory inputs result in the modulation of phase of ongoing oscillations (Howard and Poeppel, 2012; Lakatos et al., 2008, 2005; Luo et al., 2010) and the timing of inputs relative to the phase of ongoing oscillations impacts perception (Bonnefond and Jensen, 2012; Davis et al., 2020; Dugué et al., 2015; Forseth et al., 2020; Mercier et al., 2015). Based on this, we hypothesize there is a stimulus-evoked modulation of phase that spatiotemporally propagates through the human ventral visual pathway.

To probe the spread of visually-evoked phase modulation across the ventral visual stream, we utilized high spatiotemporal resolution intracranial recordings in a large human cohort (82 patients), with almost ubiquitous coverage of the ventral visual stream (1,929 electrodes), who performed a language task with relatively low visual complexity stimulus (word reading) or a memory task with a high complexity visual stimulus (face naming).

Results

82 patients semi-chronically implanted with subdural grid electrodes (SDEs; 14 patients) or stereotactically placed depth electrodes (sEEGs; 68 patients) for the localization of intractable epilepsy performed word reading (n = 40) and face naming (n = 57) tasks (Figure 1A,B). Phase modulation was quantified by computing the inter-trial phase coherence (ITC; Figure 1E,F) of the broadband low frequency signal (2-30 Hz) at each electrode, across multiple trials.
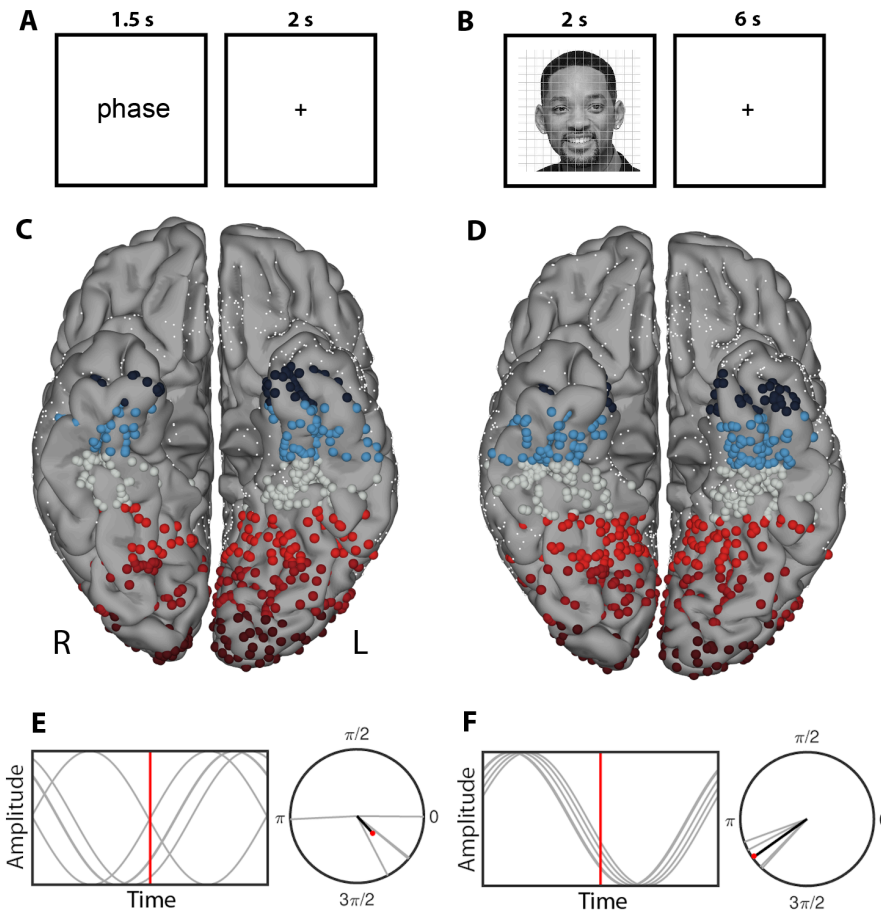

Figure 1: **Tasks, Patients and ITC Analysis.** (A,B) Schematic representation of the words (A) and faces (B) tasks. (C,D) Individual electrode locations, within the ventral ROI, for patients reading words (C; 1,059 electrodes, 40 patients) and recognizing faces (D; 1,246 electrodes, 57 patients) plotted on a standardized N27 brain. Electrode colors represent the relative locations with individual electrodes clustered into 20 mm bins along the y-axis. Smaller white spheres represent electrodes outside the ventral ROI. (E,F) Schematic representation with artificial data to illustrate low (E; ITC = 0.25) and high (F; ITC = 0.95) phase alignment along with a representation of the vector mean.

3

Phase Modulation induced by Words and Faces

Data from two representative patients, with broad coverage of ventral occipitotemporal cortex, are shown in Figure 2. In both instances, increases in inter-trial phase coherence were seen in electrodes from occipital pole to mid-fusiform cortex, for both tasks. Within each patient we also observed highly comparable patterns of ITC across both tasks. As expected, during the period preceding the onset of visual stimulation, the trial-by-trial distribution of phases at any given time was reasonably uniform. However, following presentation of a visual stimulus, they tended to a coherent center frequency (Figure 2C,D). This phase coherence persisted for approximately 2 cycles (4π rads, ~300ms) (Figure 2F,H). The temporal progression of the coherent center frequency was highly similar across both tasks.
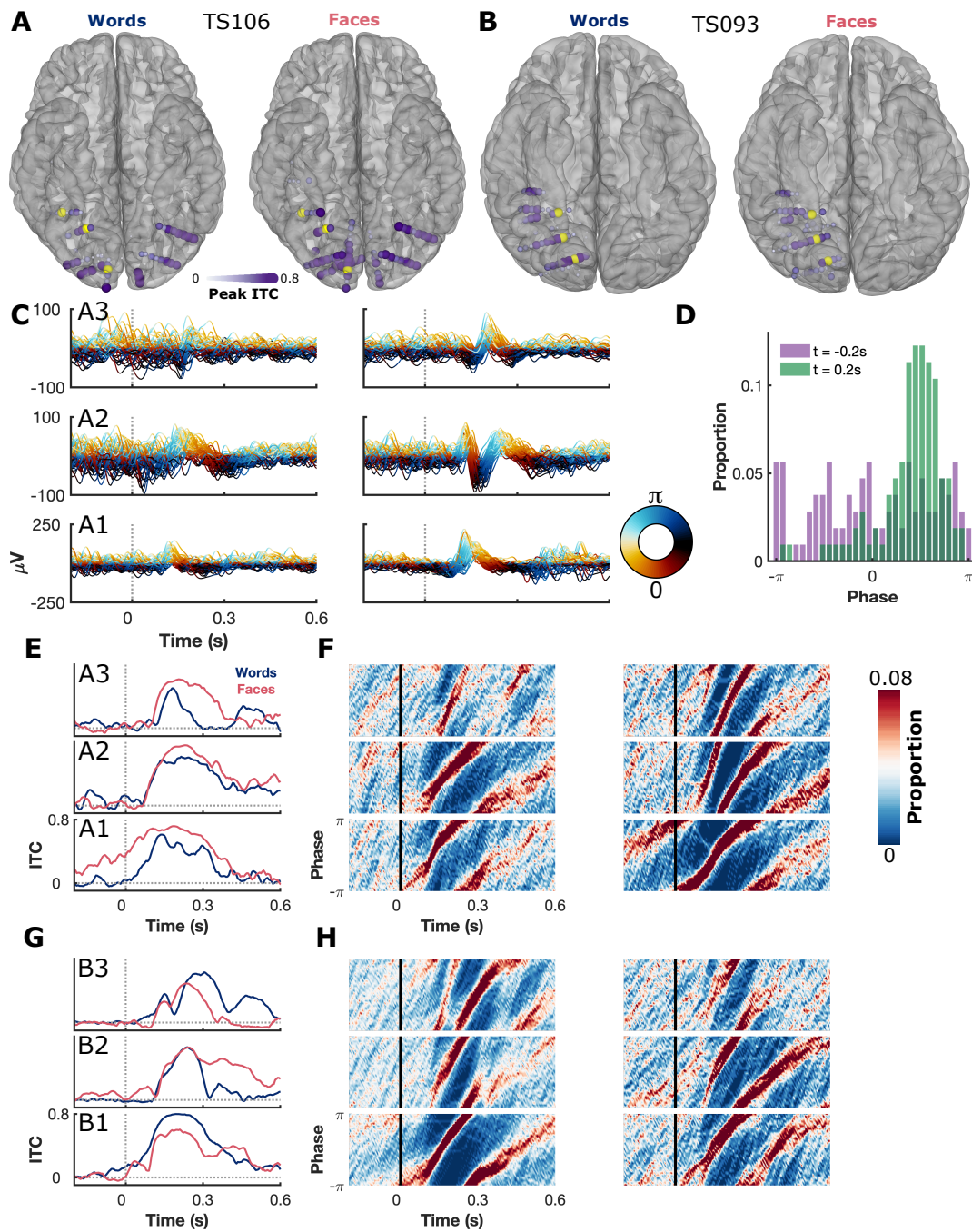
Figure 2: **Spatial Propagation of Phase Coherence in Exemplar Patients.** (A,B) ITC distributions, in native patient space, for TS106 (A) and TS093 (B). Results are shown for words (left) and faces (right). (C) Broadband low frequency (2-30 Hz) signals of 60 trials from TS106 from the words (left) and faces (right) tasks. Traces colored based on instantaneous generalized phase. (D) Phase distribution for a representative electrode at two time points during the faces task. (E-H) ITC (E,G) and phase distributions (F,H), with words (left) and faces (right) shown for three electrodes each from TS106 (E,F) and TS097 (G,H). Electrodes are highlighted in yellow in the brain plots and electrode numbers increase from posterior to anterior.

To evaluate the consistency of these effects across the population (n = 82 patients), we represented ITC amplitudes on a group normalized cortical surface from occipital pole to anterior fusiform cortex (Figure 3A,B). High ITC (>0.5) values were noted in associative cortex as far anterior as mid-fusiform. Stimulus presentation resulted in two distinct peaks of the ITC measure – a higher one around stimulus onset and a smaller one at offset. Differences in offset time between the two tasks, based on experimental design, confirmed that this was an offset response (Figure 3D,E). Results calculated using the raw signal (0.3-100Hz) showed highly correlated peak ITC with the broadband low frequency (2-30Hz) signal (Spearman correlation; words, $r(1,059) = 0.86$, $p < 0.001$; faces, $r(1,246) = 0.82$, $p < 0.001$; Supplementary Figure 1E,F) but with the raw signal displaying a longer duration of significant ITC (Supplementary Figure 1G,H).
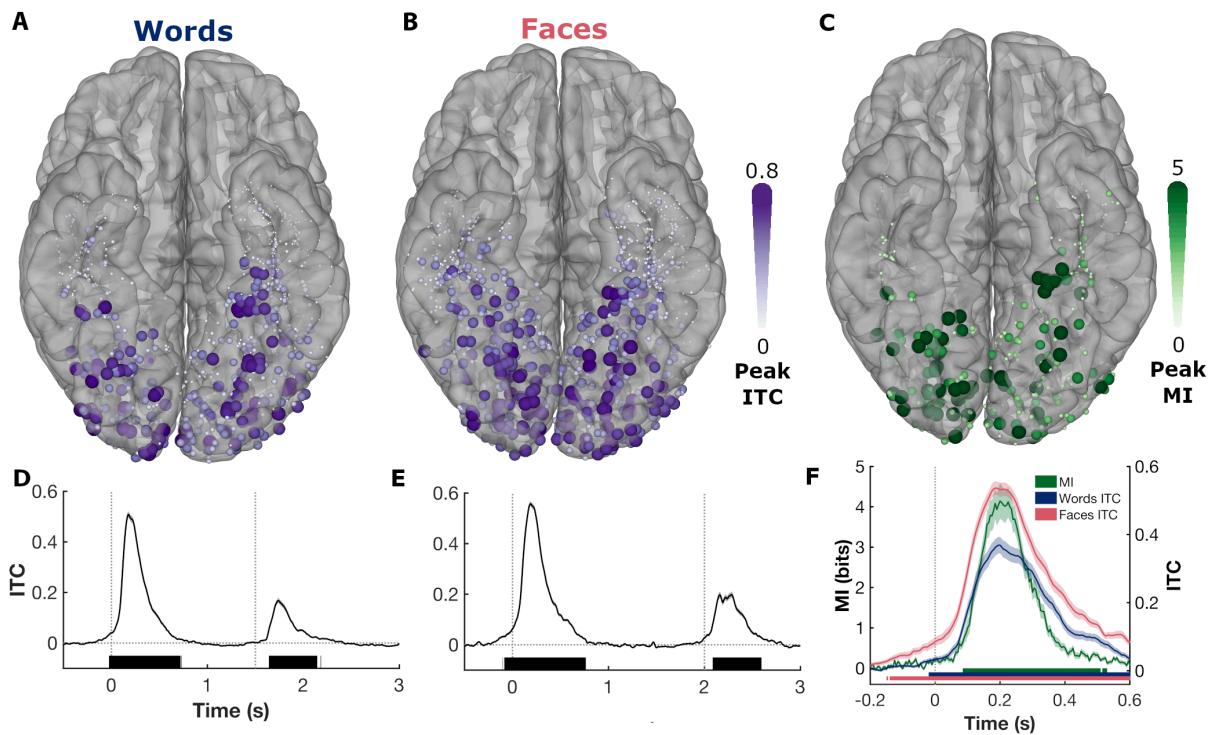
Figure 3: **Population Phase Coherence.** (A,B) Peak ITC at individual electrodes for words (A; 1,059 electrodes) and faces (B; 1,246 electrodes) tasks represented on a standardized surface. (C) Peak mutual information (MI) between the phase distributions in response to word or face presentation in patients who performed both tasks (354 electrodes, 15 patients). (D,E) Time course of ITC (mean ± SE) at electrodes with the top 20% peak amplitude ITC responses to words (D) and faces (E). Vertical lines denote the onset and offset times of each stimulus. Colored bars represent regions of significant increase over baseline (q<0.001). (F) MI and ITC for the electrodes with the top 20% highest peak MI. See also Supplementary Figures 1, 2.

6

100 The results thus far demonstrate that within each task there is phase coherence between trials and
101 the magnitude and duration of this coherence is reasonably conserved across different tasks. But,
102 how consistent is this pattern of evoked phase across tasks? To quantify this, we measured mutual
103 information (MI) in patients who performed both tasks (n = 15). We observed an increase in MI
104 following the visual onsets, representing an increase in the similarity of phase distributions between
105 tasks. This inter-task coherence peaked at ~200ms following visual onset, highly concordant with the
106 within-trial ITC (Figure 3F). 9 out of the 15 patients had at least one electrode peaking at >5 bits
107 (48/354 electrodes; Supplementary Figure 2A). Peak MI correlated well with peak ITC, measured
108 across both tasks (Spearman correlation, r(354) = 0.76, p<0.001; Supplementary Figure 2C).

109 Next, we sought to characterize the spatiotemporal properties of this response, by dividing the
110 ventral cortical surface into 20 mm bins along the y axis of the normalized surface in Talairach space,
111 and used this to compare grouped ITC profiles from each bin (Figure 4). We noted a pronounced
112 posterior-to-anterior gradient of both amplitude and onset latency of ITC with the largest responses
113 in early visual cortex and progressive diminution anteriorly in both hemispheres, for both tasks. A 4D,
114 cortical surface-based representation of the propagation of this phase coherence across the cortical
115 surface revealed a posterior-to-anterior wave, highly conserved across both tasks (Movie 1).

116

117 Movie 1: **Spread of Phase Coherence across the Cortical Surface.** Population-level, surface-based
118 representation of ITC in response to words (left) and faces (right).

119

120 To quantify this posterior-to-anterior latency gradient, we calculated the time point at which the first
121 derivative of the ITC first significantly deviated from baseline at each electrode (Figure 4E). In both
122 tasks there was a clear gradient from calcarine to anterior fusiform. Onset latency showed a
123 significant association with position in the anteroposterior axis for both words (t(781) = 12.5, β = 1.0
124 ± 0.08, p < 0.001, r^2 = 0.30) and faces (t(779) = 9.7, β = 1.3 ± 0.13, p < 0.001, r^2 = 0.21) tasks. This
125 reflects a posterior-to-anterior progression of the timing of ITC across the cortical surface from early
126 sensory cortex to associative regions and a consistent propagation rate of approximately 0.8-1 m/s
127 in Euclidean space.

128 To further investigate the spatiotemporal consistency of this effect between tasks, we analyzed just
129 the subset of patients who performed both tasks (n = 15). There was no significant difference in ITC

130 onset latency between the two tasks (t(462) = -1.6, β = -0.03 ± 0.02, p = 0.12) or any significant effect

131 of task on the propagation rate (t(462) = -1.3, β = -0.35 ± 0.27, p = 0.20).
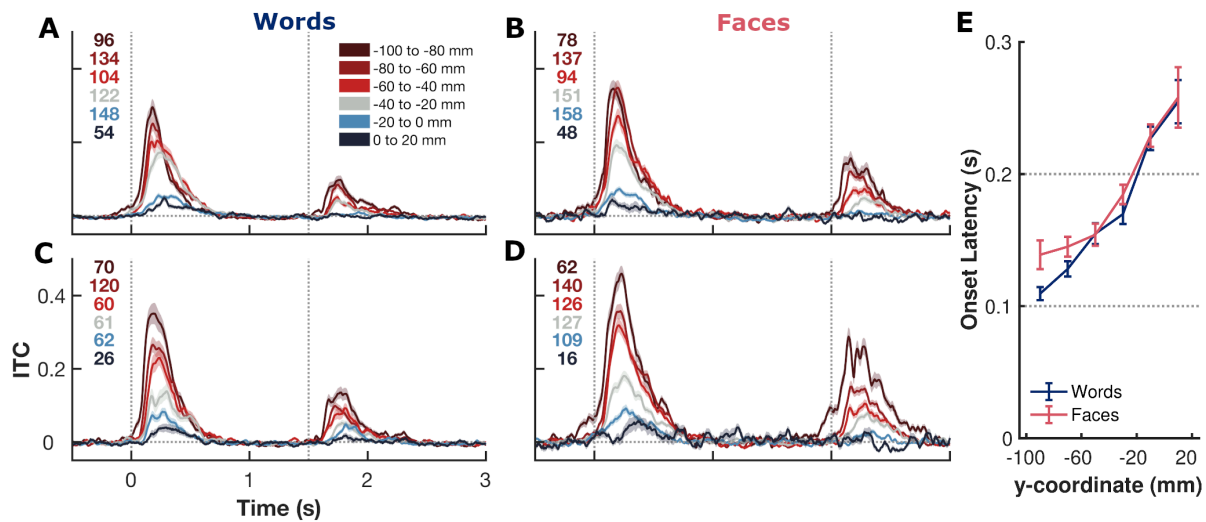

Figure 4: **ITC – Positional Analysis.** (A-D) ITC in response to words (A,C) or faces (B,D) as a function of anteroposterior position in the left (A,B) and right (C,D) hemisphere. Presented as mean ± SE. Number of electrodes in each ROI shown. Vertical lines denote stimulus onset and offset times. (E) ITC demonstrates a posterior-to-anterior gradient of first onset latency (ITC first-derivative >3.5SD deviation from baseline).

139 To further characterize this posterior-to-anterior spread and to identify the degree of propagation of

140 phase information across the cortical surface, we calculated the lagged phase locking value (PLV)

141 between pairs of electrodes. By lagging the time courses of phase progression between pairs of

142 electrodes we sought to determine to what degree the future phase of anterior sites could be

143 predicted by the current phase of posterior sites (Figure 5A). This analysis demonstrated a strong bias

144 toward a posterior-to-anterior spread of phase information, with the phase of anterior sites being

145 driven by more posterior regions (Figure 5B, Supplementary Figure 3).
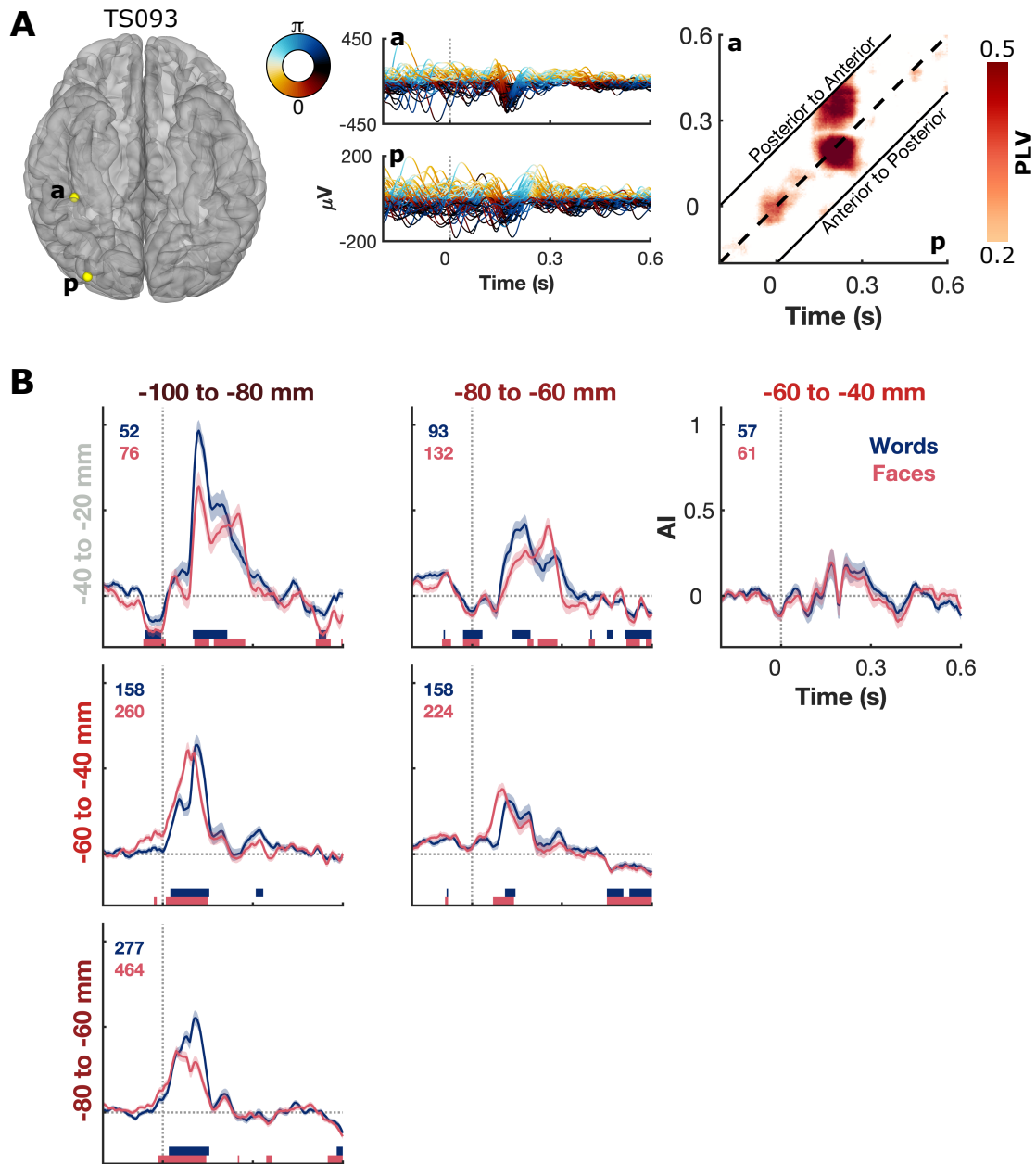
Figure 5: **Propagation of Phase.** (A) Exemplar electrode pair demonstrating the lagged phase locking value (PLV) analysis. PLV was calculated between the instantaneous phase of the posterior electrode (p) and the time lagged phase of the anterior electrode (a; -200 to 200 ms). Greater PLV above the center diagonal (dashed line) represents a greater ability to predict future phase of the anterior electrode based on the current phase of the posterior electrode. (B) Calculated asymmetry index (AI) of PLV above and below the center diagonal for high ITC (>0.5) electrode pairs across ROIs. AI > 0 represents a bias toward posterior-to-anterior phase propagation. Colored bars represent regions of significant difference from baseline (q<0.001). Number of electrode pairs in each ROI pair shown. See also Supplementary Figure 3.

Discussion

We have identified a visually-induced, macroscale, spatiotemporal propagation of phase modulation from posterior-to-anterior in human ventral occipitotemporal cortex. Strong phase modulation is seen almost ubiquitously across ventral occipitotemporal cortex in both hemispheres; from occipital pole to anterior fusiform. Following a visual event each region within the visual pathway displays a predictable, stereotyped phase progression. These findings were highly repeatable across a diverse range of visual stimuli with varying task demands and attentional loads and in only partially overlapping patient populations. We observed an approximate Euclidean propagation velocity of 0.8-1.0 m/s. This is comparable to the conduction velocities of unmyelinated horizontal projection axons in macaques (0.1-0.6 m/s) (Davis et al., 2020) and is much slower than would be expected from monosynaptic white matter transmission (>15 m/s) (Ferraina et al., 2002). This further implies that this phase propagation likely occurs via sequential cortico-cortical connections (Muller et al., 2014).

Previous work has shown the organization of spontaneous oscillations as large scale travelling waves (Bahramisharif et al., 2013; Muller et al., 2016; Zhang et al., 2018) and small scale travelling waves within early visual cortex (Muller et al., 2014; Sato et al., 2012). We expand on this work, characterizing a visually-evoked, macroscale phase propagation across the entire ventral visual pathway that likely indexes feedforward communication (Bastos et al., 2015), long-range cortico-cortical connections (Muller et al., 2014) and integration of information over broad cortical areas (Sato et al., 2012; Zhang et al., 2018).

A phase reset following visual input has been demonstrated in human (Mormann et al., 2005; Rizzuto et al., 2003; Tesche and Karhu, 2000) and macaque (Jutras et al., 2013) hippocampi. It is possible that this is also initiated as part of this sequence of ventral phase modulations. During visual exploration this hippocampal phase reset consistently occurs following saccadic eye movements (Jutras et al., 2013) suggesting that ventral phase modulation may occur following each saccade during naturalistic viewing.

Extracranial recordings of study phase modulation are an aggregate of many sources, limiting insight into underlying generators. Further, the relative inaccessibility of electrical fields generated by the ventral temporal surface (Goldenholz et al., 2009) has limited studies of visual phase modulation to early visual cortex. This has precluded insight into the spatiotemporal topography of visually-induced phase modulation in the human ventral visual pathway. Our results are supportive of the phase reset

186 model of event related potential (ERP) generation (Klimesch et al., 2007; Makeig et al., 2002; Sauseng

187 et al., 2007; Yeung et al., 2004). According to the phase reset model, the reset of instantaneous phase

188 of ongoing oscillations, tending toward a fixed value upon presentation of a stimulus, results in the

189 ERP by creating a coherent superposition of phase components (Iemi et al., 2019). Simulations of the

190 underlying generators of the ERP suggest that early components (<200 ms), corresponding to the

191 time course of ITC seen here, primarily represent feed-forward influences, with later ERP

192 components being influenced by top-down modulation (Garrido et al., 2007).

193

Conclusion

195 We demonstrate the existence of visually-induced macroscale posterior-to-anterior propagation of

196 phase modulation across the human ventral occipitotemporal cortex. We propose this represents a

197 feed-forward spread of information via horizontal cortico-cortical connections throughout the

198 ventral visual pathway.

199

Materials and Methods

201 *Participants*: 82 patients (44 male, 18-60 years, 16 left-handed) undergoing implantation with

202 intracranial electrodes for seizure localization of pharmaco-resistant epilepsy participated after

203 giving written informed consent. Participants with significant additional neurological history (e.g.

204 previous resections, MR imaging abnormalities such as malformations or hypoplasia) were excluded.

205 All experimental procedures were reviewed and approved by the Committee for the Protection of

206 Human Subjects (CPHS) of the University of Texas Health Science Center at Houston as Protocol

207 Number HSC-MS-06-0385.

208 *Electrode Implantation and Data Recording:* Data were acquired using either subdural grid electrodes

209 (SDEs; 14 patients) or stereotactically placed depth electrodes (sEEGs; 68 patients). SDEs were

210 subdural platinum-iridium electrodes embedded in a silicone elastomer sheet (PMT Corporation; top-

211 hat design; 3mm diameter cortical contact), surgically implanted via a craniotomy following

212 previously described methods (Pieters et al., 2013; Tandon, 2012; Tong et al., 2020). sEEGs were

213 implanted using a Robotic Surgical Assistant (ROSA; Medtech, Montpellier, France) (Rollo et al., 2020;

214 Tandon et al., 2019). Each sEEG probe (PMT corporation, Chanhassen, Minnesota) is 0.8 mm in

11

215 diameter, with 8-16 electrode contacts, each contact being a 2mm long platinum-iridium cylinder

216 separated from the adjacent contact by 1.5 - 2.43 mm. Each patient had 12-20 such probes

217 implanted. Following surgical implantation, electrodes were localized by co-registration of pre-

218 operative anatomical 3T MRI and post-operative CT scans in AFNI (Cox, 1996). Electrode positions

219 were projected onto a cortical surface model generated in FreeSurfer (Dale et al., 1999), and

220 displayed on the cortical surface model for visualization (Pieters et al., 2013). Intracranial data were

221 collected during research experiments starting on the first day after electrode implantation for sEEGs

222 and two days after implantation for SDEs. Data were digitized at 2 kHz using the NeuroPort recording

223 system (Blackrock Microsystems, Salt Lake City, Utah), imported into Matlab, and visually inspected

224 for line noise, artifacts and epileptic activity. Of a total of 11,164 electrodes, 3,919 electrodes with

225 obvious line noise or localized in proximity to sites of seizure onset were excluded. Each electrode

226 was re-referenced to the common average of the remaining channels. Trials contaminated by inter-

227 ictal epileptic spikes were discarded.

228 *Signal Analysis:* An ROI encompassing the entire occipital lobe and the ventral temporal surface, but

229 excluding parahippocampal and entorhinal regions, was then applied, restricting us to 1,929

230 electrodes which form the basis of this work. These electrodes were grouped into sub-ROIs within 20

231 mm intervals along the y-axis of Talairach space, from -100 mm to 20 mm (Figure 1D-F).

232 Raw data was notch filtered to remove line noise (zero-phase 2nd order Butterworth band-stop

233 filters). Phase information was extracted from the down-sampled (200 Hz) and wide band-pass

234 filtered data (2 – 30 Hz; zero-phase 8th order Butterworth band-pass filter) using the 'generalized

235 phase' method (Davis et al., 2020) with a single-sided Fourier transform approach (Marple, 1999).

236 This method captures the phase of the predominant fluctuations in the wideband signal and

237 minimizes filter-related distortion of the waveform.

238 Inter-trial Phase Coherence (ITC) was calculated as the absolute vector length of the mean of unit

239 vectors with the instantaneous phase of stimulus-aligned trials (Figure 1G,H). Phase locking value

240 (PLV) was calculated identically to ITC but instead using phase difference between two electrodes.

241 ITC and PLV were computed as the median value of 50 iterations of a random 60 trials. ITC and PLV

242 were baselined -1,000 to -100 ms before each stimulus. PLV was calculated between pairs of

243 electrodes in separate ROIs, within patient, within hemisphere. PLV statistics were performed using

244 a bootstrapped null distribution, randomly re-pairing trials between electrodes, using 5,000

245 repetitions. Phase probability distributions were quantified, using 30 equally spaced bins between -

246   π and π, and mutual information (MI) was calculated based on these distributions at each time point,

247   baselined -1,000 to -100ms before each stimulus. Asymmetry index (AI) was calculated based on the

248   lagged PLV results at each time point as $AI = log_2(PLV_{pa}/PLV_{ap})$, where PLV_{pa} represents the mean PLV

249   between electrode p at time t and electrode a between time t and time $t + 200$ ms.

250   <u>Experimental Design and Statistical Analysis:</u> Patients read single words (n = 40 patients) or identified

251   celebrity faces (n = 57 patients). Stimuli were presented on a 2,880 x 1,800, 15.4" LCD screen

252   positioned at eye-level, 2-3' from the patient. Additional details of each experiment are below:

253   *Word Reading:* Participants read aloud monosyllabic words (e.g. dream) and pseudowords (e.g.

254   meech) presented in lower-case Arial font, 150 pixels high (~2.2° visual angle) (Figure 1A)

255   (Woolnough et al., 2021a). Stimuli were presented using Psychophysics Toolbox (Kleiner et al.,

256   2007) run in Matlab. Each stimulus was displayed for 1,500 ms with an inter-stimulus interval of

257   2,000 ms. Stimuli were presented in two recording sessions, each with 160 stimuli in a

258   pseudorandom order with no repeats.

259   *Face Recognition:* Participants were presented with greyscale photos of famous faces and asked to

260   name them aloud (Figure 1B) (Kadipasaoglu et al., 2017; Woolnough et al., 2020). Stimuli were

261   matched for luminance and contrast and presented, using Python 2.7, at a size of 500 x 500 pixels

262   (~7.5° visual angle) for 2,000 ms, with an inter-stimulus interval of 6,000 ms. Stimuli were presented

263   in one recording session, with 60-125 faces presented in pseudorandom order with no repeats.

264   Participants who correctly identified less than 20 stimuli were excluded.

265   Linear regressions were performed using robust regression models (Matlab function *fitlm* using

266   *'RobustOpts'*; iteratively reweighted least squares with bisquare weighting) (Welsch, 1977), to

267   minimize the effect of outliers and to make fewer assumptions than traditional least squares linear

268   regression models. To calculate onset latencies, we determined the first time point per electrode,

269   within 600 ms of stimulus onset, where the first derivative of the ITC exceeded 3.5 standard

270   deviations (~p<0.001) from baseline. We then used a regression model, predicting onset latency

271   based on position in the y (anteroposterior) axis, derived from the surface-based co-registration. All

272   temporal analyses were corrected for multiple comparisons using a Benjamini-Hochberg false-

273   detection rate (FDR) threshold of q<0.001.

Acknowledgements

Author Contributions

Conceptualization: OW, NT; Methodology: OW, NT; Data curation: OW, PSR, ZR; Software: OW; Formal Analysis and Visualization: OW; Writing – Original Draft: OW; Writing – Review and Editing: OW, KJF, NT; Funding Acquisition: NT; Neurosurgical Procedures: NT.

Declaration of Interests

The authors declare no competing interests

References

Alamia A, VanRullen R. 2019. Alpha oscillations and traveling waves: Signatures of predictive coding? *PLoS Biol* **17**. doi:10.1371/journal.pbio.3000487

Arnal LH, Giraud AL. 2012. Cortical oscillations and sensory predictions. *Trends Cogn Sci* **16**:390–398. doi:10.1016/j.tics.2012.05.003

Bahramisharif A, van Gerven MAJ, Aarnoutse EJ, Mercier MR, Schwartz TH, Foxe JJ, Ramsey NF, Jensen O. 2013. Propagating neocortical gamma bursts are coordinated by traveling alpha waves. *J Neurosci* **33**:18849–18854. doi:10.1523/JNEUROSCI.2455-13.2013

Bastos AM, Vezoli J, Bosman CA, Schoffelen JM, Oostenveld R, Dowdall JR, DeWeerd P, Kennedy H, Fries P. 2015. Visual areas exert feedforward and feedback influences through distinct frequency channels. *Neuron* **85**:390–401. doi:10.1016/j.neuron.2014.12.018

Bonnefond M, Jensen O. 2012. Alpha oscillations serve to protect working memory maintenance against anticipated distracters. *Curr Biol* **22**:1969–1974. doi:10.1016/j.cub.2012.08.029

Cox RW. 1996. AFNI: Software for Analysis and Visualization of Functional Magnetic Resonance Neuroimages. *Comput Biomed Res* **29**:162–173. doi:10.1006/cbmr.1996.0014

Dale AM, Fischl B, Sereno MI. 1999. Cortical Surface-Based Analysis: I. Segmentation and Surface Reconstruction. *Neuroimage* **9**:179–194. doi:10.1006/nimg.1998.0395

Davis Z, Muller L, Trujillo J-M, Sejnowski T, Reynolds J. 2020. Spontaneous Traveling Cortical Waves Gate Perception in Awake Behaving Primates. *Nature*. doi:10.1038/s41586-020-2802-y

Dugué L, Marque P, VanRullen R. 2015. Theta oscillations modulate attentional search performance periodically. *J Cogn Neurosci* **27**:945–958. doi:10.1162/jocn_a_00755

Felleman DJ, Van Essen DC. 1991. Distributed Hierarchical Processing in the Primate Cerebral Cortex. *Cereb Cortex* **1**:1–47. doi:10.1093/cercor/1.1.1

Ferraina S, Paré M, Wurtz RH. 2002. Comparison of cortico-cortical and cortico-collicular signals for the generation of saccadic eye movements. *J Neurophysiol* **87**:845–858. doi:10.1152/jn.00317.2001

Forseth KJ, Hickok G, Rollo PS, Tandon N. 2020. Language prediction mechanisms in human auditory cortex. *Nat Commun* **11**:5240. doi:10.1038/s41467-020-19010-6

15

315 Forseth KJ, Kadipasaoglu CM, Conner CR, Hickok G, Knight RT, Tandon N. 2018. A lexical semantic

316   hub for heteromodal naming in middle fusiform gyrus. *Brain* **141**:2112–2126.

317   doi:10.1093/brain/awy120

318 Garrido MI, Kilner JM, Kiebel SJ, Friston KJ. 2007. Evoked brain responses are generated by

319   feedback loops. *Proc Natl Acad Sci U S A* **104**:20961–20966. doi:10.1073/pnas.0706274105

320 Ghuman AS, Brunet NM, Li Y, Konecky RO, Pyles JA, Walls SA, Destefino V, Wang W, Richardson RM.

321   2014. Dynamic encoding of face information in the human fusiform gyrus. *Nat Commun*

322   **5**:5672. doi:10.1038/ncomms6672

323 Goldenholz DM, Ahlfors SP, Hämäläinen MS, Sharon D, Ishitobi M, Vaina LM, Stufflebeam SM. 2009.

324   Mapping the signal-to-noise-ratios of cortical sources in magnetoencephalography and

325   electroencephalography. *Hum Brain Mapp* **30**:1077–1086. doi:10.1002/hbm.20571

326 Halgren M, Ulbert I, Bastuji H, Fabó D, Eross L, Rey M, Devinsky O, Doyle WK, Mak-McCully R,

327   Halgren E, Wittner L, Chauvel P, Heit G, Eskandar E, Mandell A, Cash SS. 2019. The generation

328   and propagation of the human alpha rhythm. *Proc Natl Acad Sci* **116**:23772–23782.

329   doi:10.1073/pnas.1913092116

330 Hirshorn EA, Li Y, Ward MJ, Richardson RM, Fiez JA, Ghuman AS. 2016. Decoding and disrupting left

331   midfusiform gyrus activity during word reading. *Proc Natl Acad Sci* **113**:8162–8167.

332   doi:10.1073/pnas.1604126113

333 Howard MF, Poeppel D. 2012. The neuromagnetic response to spoken sentences: Co-modulation of

334   theta band amplitude and phase. *Neuroimage* **60**:2118–2127.

335   doi:10.1016/j.neuroimage.2012.02.028

336 Iemi L, Busch NA, Laudini A, Haegens S, Samaha J, Villringer A, Nikulin V V. 2019. Multiple

337   mechanisms link prestimulus neural oscillations to sensory responses. *Elife* **8**:1–34.

338   doi:10.1101/461558

339 Jutras MJ, Fries P, Buffalo EA. 2013. Oscillatory activity in the monkey hippocampus during visual

340   exploration and memory formation. *Proc Natl Acad Sci* **110**:13144–13149.

341   doi:10.1073/pnas.1302351110

342 Kadipasaoglu CM, Conner CR, Baboyan VG, Rollo M, Pieters TA, Tandon N. 2017. Network dynamics

343   of human face perception. *PLoS One* **12**. doi:10.1371/journal.pone.0188834

344 Kadipasaoglu CM, Conner CR, Whaley ML, Baboyan VG, Tandon N. 2016. Category-selectivity in
345   human visual cortex follows cortical topology: A grouped icEEG study. *PLoS One* **11**.
346   doi:10.1371/journal.pone.0157109

347 Kleiner M, Brainard D, Pelli D. 2007. What's new in Psychtoolbox-3? *Perception* **36**.
348   doi:10.1068/v070821

349 Klimesch W, Sauseng P, Hanslmayr S, Gruber W, Freunberger R. 2007. Event-related phase
350   reorganization may explain evoked neural dynamics. *Neurosci Biobehav Rev* **31**:1003–1016.
351   doi:10.1016/j.neubiorev.2007.03.005

352 Lakatos P, Karmos G, Mehta AD, Ulbert I, Schroeder CE. 2008. Entrainment of neuronal oscillations
353   as a mechanism of attentional selection. *Science (80-)* **320**:110–113.
354   doi:10.1126/science.1154735

355 Lakatos P, Shah AS, Knuth KH, Ulbert I, Karmos G, Schroeder CE. 2005. An oscillatory hierarchy
356   controlling neuronal excitability and stimulus processing in the auditory cortex. *J Neurophysiol*
357   **94**:1904–1911. doi:10.1152/jn.00263.2005

358 Lamme VAF, Roelfsema PR. 2000. The distinct modes of vision offered by feedforward and
359   recurrent processing. *Trends Neurosci* **23**:571–579. doi:10.1016/S0166-2236(00)01657-X

360 Lozano-Soldevilla D, VanRullen R. 2019. The Hidden Spatial Dimension of Alpha: 10-Hz Perceptual
361   Echoes Propagate as Periodic Traveling Waves in the Human Brain. *Cell Rep* **26**:374–380.
362   doi:10.1016/j.celrep.2018.12.058

363 Luo H, Liu Z, Poeppel D. 2010. Auditory cortex tracks both auditory and visual stimulus dynamics
364   using low-frequency neuronal phase modulation. *PLoS Biol* **8**:25–26.
365   doi:10.1371/journal.pbio.1000445

366 Makeig S, Westerfield M, Jung TP, Enghoff S, Townsend J, Courchesne E, Sejnowski TJ. 2002.
367   Dynamic brain sources of visual evoked responses. *Science (80-)* **295**:690–694.
368   doi:10.1126/science.1066168

369 Marple SL. 1999. Computing the discrete-time "analytic" signal via FFT. *IEEE Trans Signal Process*
370   **47**:2600–2603. doi:10.1109/acssc.1997.679118

371 Mercier MR, Molholm S, Fiebelkorn IC, Butler JS, Schwartz TH, Foxe JJ. 2015. Neuro-oscillatory
372   phase alignment drives speeded multisensory response times: An electro-corticographic

373   investigation. *J Neurosci* **35**:8546–8557. doi:10.1523/JNEUROSCI.4527-14.2015

374   Mishkin M, Ungerleider LG, Macko KA. 1983. Object vision and spatial vision: two cortical pathways.

375   *Trends Neurosci* **6**:414–417. doi:10.1016/0166-2236(83)90190-X

376   Morán MA, Mufson EJ, Mesulam M -M. 1987. Neural inputs into the temporopolar cortex of the

377   rhesus monkey. *J Comp Neurol* **256**:88–103. doi:10.1002/cne.902560108

378   Mormann F, Fell J, Axmacher N, Weber B, Lehnertz K, Elger CE, Fernández G. 2005.

379   Phase/amplitude reset and theta-gamma interaction in the human medial temporal lobe

380   during a continuous word recognition memory task. *Hippocampus* **15**:890–900.

381   doi:10.1002/hipo.20117

382   Muller L, Chavane F, Reynolds J, Sejnowski TJ. 2018. Cortical travelling waves: Mechanisms and

383   computational principles. *Nat Rev Neurosci* **19**:255–268. doi:10.1038/nrn.2018.20

384   Muller L, Piantoni G, Koller D, Cash SS, Halgren E, Sejnowski TJ. 2016. Rotating waves during human

385   sleep spindles organize global patterns of activity that repeat precisely through the night. *Elife*

386   **5**. doi:10.7554/elife.17267

387   Muller L, Reynaud A, Chavane F, Destexhe A. 2014. The stimulus-evoked population response in

388   visual cortex of awake monkey is a propagating wave. *Nat Commun* **5**.

389   doi:10.1038/ncomms4675

390   Pieters TA, Conner CR, Tandon N. 2013. Recursive grid partitioning on a cortical surface model: an

391   optimized technique for the localization of implanted subdural electrodes. *J Neurosurg*

392   **118**:1086–1097. doi:10.3171/2013.2.JNS121450

393   Rizzuto DS, Madsen JR, Bromfield EB, Schulze-Bonhage A, Seelig D, Aschenbrenner-Scheibe R,

394   Kahana MJ. 2003. Reset of human neocortical oscillations during a working memory task. *Proc*

395   *Natl Acad Sci* **100**:7931–6. doi:10.1073/pnas.0732061100

396   Rollo PS, Rollo MJ, Zhu P, Woolnough O, Tandon N. 2020. Oblique trajectory angles in robotic

397   stereo-electroencephalography. *J Neurosurg*. doi:10.3171/2020.5.JNS20975

398   Sato TK, Nauhaus I, Carandini M. 2012. Traveling Waves in Visual Cortex. *Neuron* **75**:218–229.

399   doi:10.1016/j.neuron.2012.06.029

400   Sauseng P, Klimesch W, Gruber WR, Hanslmayr S, Freunberger R, Doppelmayr M. 2007. Are event-

401   related potential components generated by phase resetting of brain oscillations? A critical

402   discussion. *Neuroscience* **146**:1435–1444. doi:10.1016/j.neuroscience.2007.03.014

403   Tandon N. 2012. Mapping of human language In: Yoshor D, Mizrahi E, editors. Clinical Brain

404   Mapping. McGraw Hill Education. pp. 203–218.

405   Tandon N, Tong BA, Friedman ER, Johnson JA, Von Allmen G, Thomas MS, Hope OA, Kalamangalam

406   GP, Slater JD, Thompson SA. 2019. Analysis of Morbidity and Outcomes Associated With Use of

407   Subdural Grids vs Stereoelectroencephalography in Patients With Intractable Epilepsy. *JAMA*

408   *Neurol* **76**:672–681. doi:10.1001/jamaneurol.2019.0098

409   Tang H, Buia C, Madhavan R, Crone NE, Madsen JR, Anderson WS, Kreiman G. 2014. Spatiotemporal

410   Dynamics Underlying Object Completion in Human Ventral Visual Cortex. *Neuron* **83**:736–748.

411   doi:10.1016/j.neuron.2014.06.017

412   Tesche CD, Karhu J. 2000. Theta oscillations index human hippocampal activation during a working

413   memory task. *Proc Natl Acad Sci* **97**:919–924. doi:10.1073/pnas.97.2.919

414   Tong BA, Esquenazi Y, Johnson J, Zhu P, Tandon N. 2020. The Brain is Not Flat: Conformal Electrode

415   Arrays Diminish Complications of Subdural Electrode Implantation, A Series of 117 Cases.

416   *World Neurosurg* **144**:e734–e742. doi:10.1016/j.wneu.2020.09.063

417   Welsch RE. 1977. Robust regression using iteratively reweighted least-squares. *Commun Stat -*

418   *Theory Methods* **6**:813–827. doi:10.1080/03610927708827533

419   Woolnough O, Donos C, Curtis A, Rollo PS, Roccaforte ZJ, Tandon N. 2021a. A Spatiotemporal Map

420   of Reading Aloud. *bioRxiv*. doi:10.1101/2021.05.23.445307

421   Woolnough O, Donos C, Rollo PS, Forseth KJ, Lakretz Y, Crone NE, Fischer-Baum S, Dehaene S,

422   Tandon N. 2021b. Spatiotemporal dynamics of orthographic and lexical processing in the

423   ventral visual pathway. *Nat Hum Behav* **5**:389–398. doi:10.1038/s41562-020-00982-w

424   Woolnough O, Rollo PS, Forseth KJ, Kadipasaoglu CM, Ekstrom AD, Tandon N. 2020. Category

425   Selectivity for Face and Scene Recognition in Human Medial Parietal Cortex. *Curr Biol* **30**:2707–

426   2715. doi:10.1016/j.cub.2020.05.018

427   Yeung N, Bogacz R, Holroyd CB, Cohen JD. 2004. Detection of synchronized oscillations in the

428   electroencephalogram: An evaluation of methods. *Psychophysiology* **41**:822–832.

429   doi:10.1111/j.1469-8986.2004.00239.x

430   Zhang H, Watrous AJ, Patel A, Jacobs J. 2018. Theta and Alpha Oscillations Are Traveling Waves in

431   the Human Neocortex. *Neuron* **98**:1269–1281. doi:10.1016/j.neuron.2018.05.019

432

433 **Supplementary Figures**
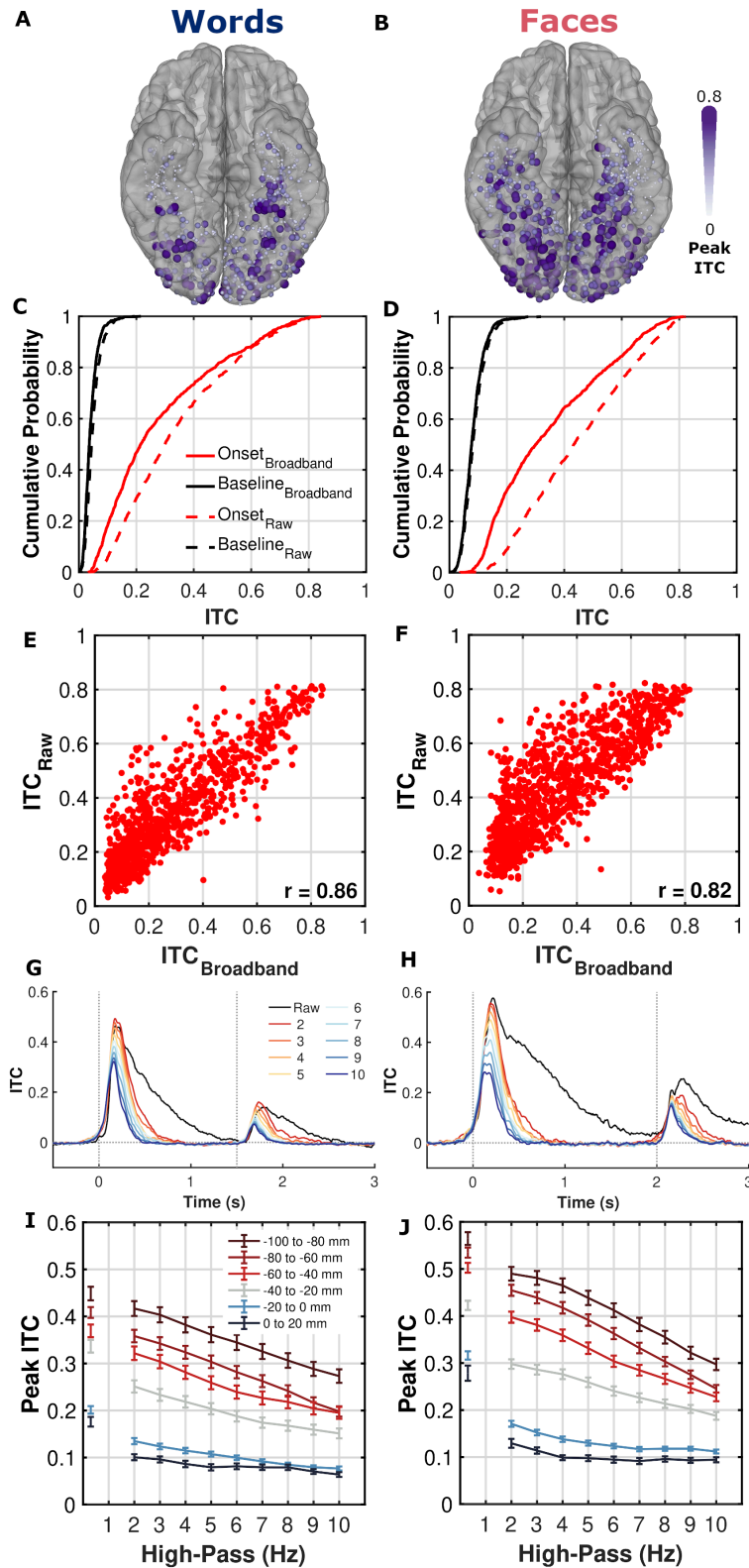
434

435 Supplementary Figure 1: **Comparison of Broadband Low Frequency and Raw Signal Analyses.** (A,B)

436 Spatial distribution of peak ITC for each electrode in the raw (0.3 – 100 Hz) signal. (C,D) Cumulative

437 probability distribution of raw and broadband ITC. (E,F) Relationship of raw and broadband ITC.

438   (G,H) Temporal ITC profile with varying high pass filter parameters. Same electrodes as Figure 3D,E.

439   (I,J) Changes in peak ITC within each spatial ROI for the raw signal (0.3 Hz high pass) and varying

440   high pass filtered signals (2 - 10Hz). Analyses shown for the words (A,C,E,G,I) and faces (B,D,F,H,J)

441   tasks.

442
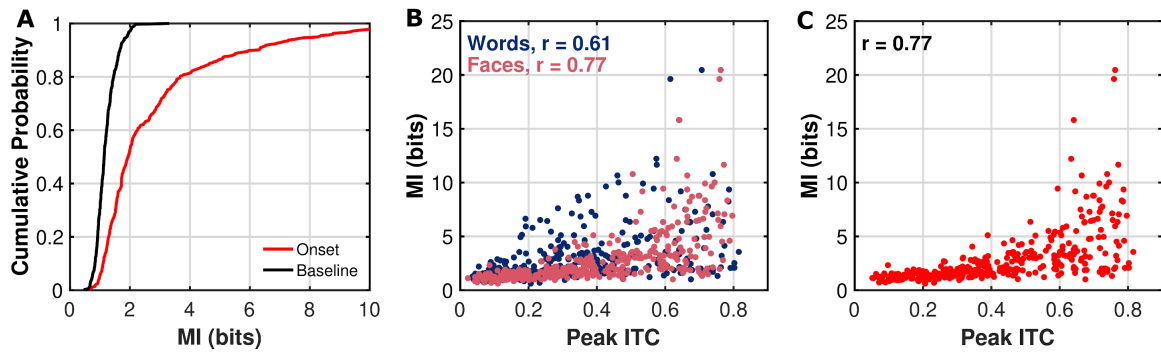
444   Supplementary Figure 2: **Distribution of Mutual Information (MI).** (A) Cumulative distribution

445   function of peak MI within the onset window (0 to 600 ms; red) or during the baseline window (-

446   500 to -100 ms; black). (B,C) Relationship between peak MI and (B) peak ITC in the words and faces

447   tasks or (C) peak ITC across both tasks, within individual electrodes.

448
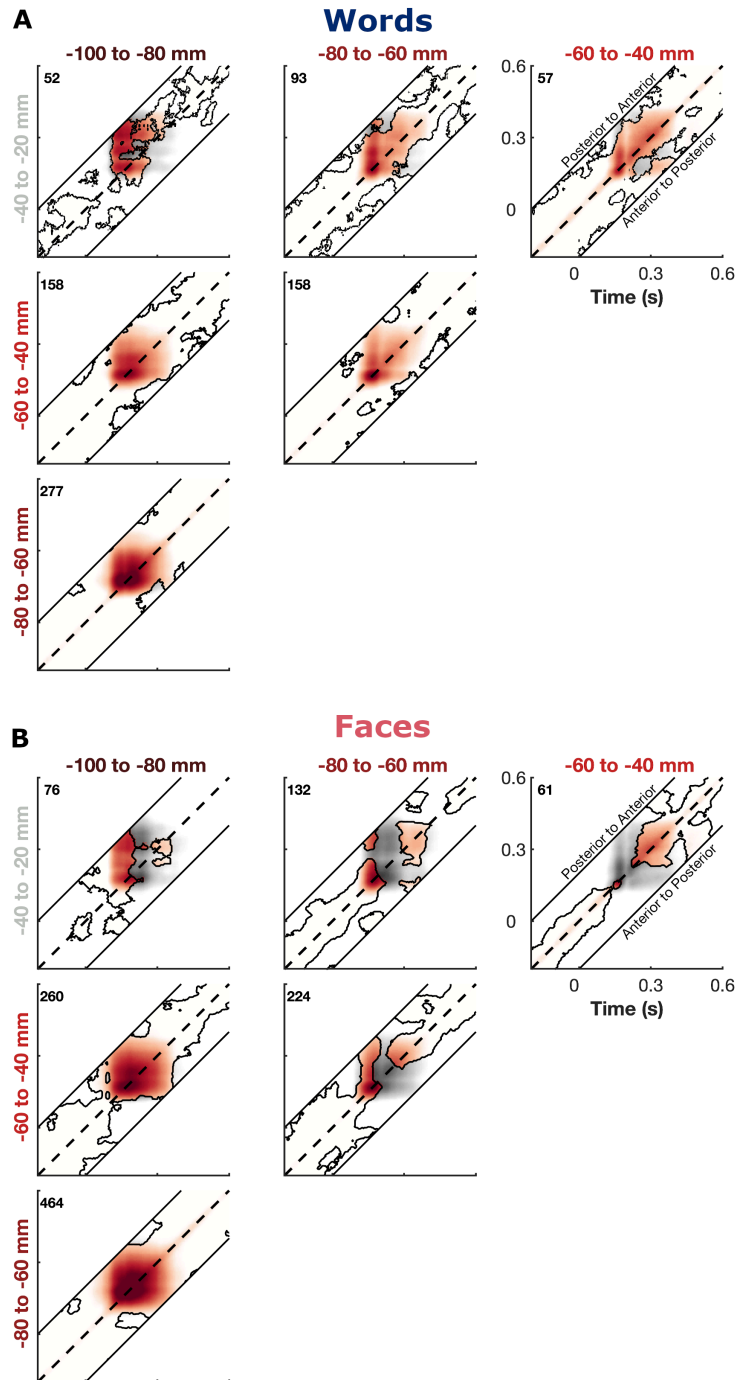
Supplementary Figure 3: **Lagged Phase Locking Value.** PLV was calculated between the instantaneous phase of the posterior electrodes (columns) and the time lagged phase of the anterior electrodes (rows; -200 to 200 ms) for the words (A) and faces (B) tasks. Greater PLV above the center diagonal (dashed line) represents a greater ability to predict future phase of the anterior electrodes based on the current phase of the posterior electrodes. Areas of significant PLV (q< 0.05) above a trial shuffled null distribution are indicated by contours and non-significant areas are desaturated. Number of electrode pairs in each ROI pair shown.